Since January 2020 Elsevier has created a COVID-19 resource centre with free information in English and Mandarin on the novel coronavirus COVID-19. The COVID-19 resource centre is hosted on Elsevier Connect, the company's public news and information website.

Polyhedron 233 (2023) 116304

Contents lists available at ScienceDirect

Polyhedron

journal homepage: www.elsevier.com/locate/poly

Molecular docking with SARS-CoV-2 and potential drug property of a bioactive novel Zn(II) polymer: A combined experimental and theoretical study

Swah Mohd. Nashre-ul-Islam [a,*], Kamala Kanta Borah [a], Muhammad Asam Raza [b], Füreya Elif Öztürkkan [c,*]

[a] Department of Chemistry, Mangaldai College, Assam 784125, India
[b] Department of Chemistry, Hafiz Hayat Campus, University of Gujrat, Gujrat, Pakistan
[c] Department of Chemical Engineering, Kafkas University, Kars, Turkey

ARTICLE INFO

Keywords:
Zn(II) polymer
Hirshfeld surface analysis
Theoretical study
Molecular docking
ADMET calculation

ABSTRACT

A new Zn(II) coordination polymer based on *o*-phthalato (Phth) and 2-aminopyridine (2-Ampy) viz. {[Zn(2-Ampy)$_2$(Phth)]•(H$_2$O)]}$_n$ (**1**) has been synthesized at room temperature and characterized by elemental analyses, electronic spectroscopy, FT-IR spectroscopy, thermal analysis (TGA/DSC), powder X-ray diffraction (PXRD) and single crystal X-ray diffraction. The basic trimeric units of **1** form a polymeric chain by N—H···O and π···π interactions. These polymeric chains interconnect through various non-covalent interactions in two perpendicular directions to ultimately give rise to a 3D architecture of **1**. The interesting non-covalent interactions in **1**, contributing to its stability in the solid state are studied by Hirshfeld surface analysis and other different theoretical tools. Molecular docking study of **1** is performed against six different proteins of SARS-CoV-2. The drug potential of the synthesized compound is evaluated by ADMET calculations.

1. Introduction

The term "coordination polymer" (CP) was first introduced by R. C. Burrows and J. C. Bailar Jr. [1]. However, it was only after the Australian chemist Robson's report on the crystal structures of a series of porous coordination polymers with ion-exchange capability that this emerging field captured the attention of chemists worldwide. This wide scientific attention arises not only from their fascinating topologies and structures [2–4], but also from their high potential applications in as diverse fields as gas adsorption and separation [5], luminescent materials [6], and catalysis [7] etc [8,9]. The CPs are assembled by fusing inorganic vertices (metal ions or metal clusters) and organic ligands via coordination bonds (or even supramolecular interactions). They usually feature a highly ordered structure with repeating coordination entities extending in at least one dimension [10]. This inorganic–organic hybrid nature of the CPs gives rise to their diverse structures and properties thereby contributing a lot to their versatility. As such, new CPs are being extensively investigated for unique structures and specific functions and numerous strategies and methods have been employed accordingly [11–13].

Despite the considerable progress achieved so far in this field, the assembly of coordination polymers in the desired way is not that easy. This is because the assembly of such compounds is influenced by various factors, such as the nature and coordination properties of the metal nodes [14,15], type and connectivity of organic building blocks [16,17], stoichiometry and reaction conditions [18,19], effects of templates [20–22] or supporting ligands [23,24].

Various aromatic polycarboxylic acids have been extensively used as multifunctional building blocks in designing novel polymeric structures [25,26]. Among them, the *o*-phthalic acid (H$_2$Phth) is a well-known versatile ligand, which is capable of chelating as well as bridging metal ions, thereby leading to the formation of polynuclear and low-dimensional systems [27,28]. The H$_2$Pht and its anions, HPhth$^-$ and Phth^{2-} can adopt a very wide variety of coordination modes with metal centers. The subtle interplay between steric hindrance arising out of the proximity of the two carboxylate groups and the tendency of the phthalates to form the largest possible number of metal–oxygen bonds upon complexation leads to the wide variety of observed architectures. So far, twenty-six different coordination modes have been observed in the crystal structures of various metal complexes involving this ligand

* Corresponding authors.
E-mail addresses: smnashreulislam@gmail.com (S.Mohd. Nashre-ul-Islam), elif@kafkas.edu.tr (F.E. Öztürkkan).

https://doi.org/10.1016/j.poly.2023.116304
Received 14 November 2022; Accepted 18 January 2023
Available online 21 January 2023

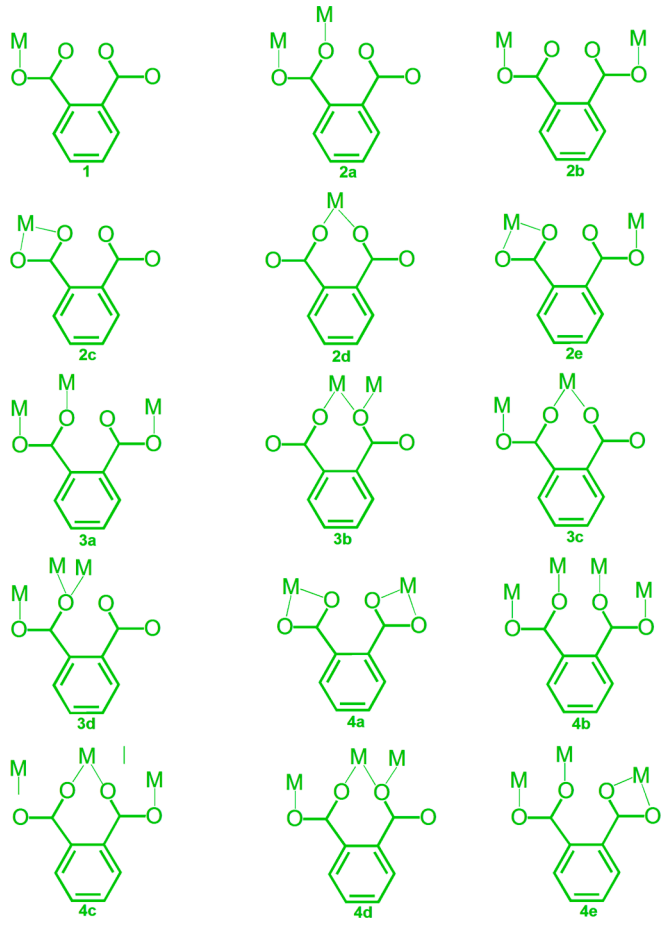

Scheme 1. A few of the wide variety of coordination modes adopted by the phthalate ion. *1*: monodentate, *2*: bidentate, *3*: tridentate, *4*: tetradentate.

[Scheme 1]. Out of these, the 1,6-bridging mode [*2b* in Scheme 1] is the most common, which favors the formation of coordination polymers [29].

Similarly, pyridine and its derivatives are widely used in the design and synthesis of multifunctional compounds with important biological and pharmacological applications [30]. Amongst the pyridine derivatives, 2-aminopyridine (2-Ampy)–a potential bidentate ligand with two *N*-donor atoms–is pharmacologically important because of its use in the synthesis of various pharmaceuticals [31]. The major advantage of this ligand is its simple design, which can be utilized to produce a single product with minimum side reactions [32]. 2-Aminopyridine mainly acts as a monodentate ligand through its pyridine *N*-atom [33,34]. This favors the formation of additional H-bonds through the exocyclic amine *N*-atom. Less commonly, it can coordinate with the central metal through the exocyclic amino *N*-atom [35] and form chelates with a bidentate coordination mode through both the pyridine N- and exocyclic amine *N*-atoms [36].

There are a number of unusually short interactions, which could affect the crystal packing and molecular structure in the solid state. One such interaction is the C—H···H—C interactions, which occur in the distance range of 1.7–2.4 Å. Despite their very weak nature, they can produce sufficient stabilization effects for maintaining sterically strained conformations and affecting the physical properties of compounds to a greater extent. These attractive intermolecular interactions, -occurring between identically or similarly charged hydrogen atoms, -have closed-shell, donor–acceptor and van der Waals nature. These H···H interactions are different from a "dihydrogen bond", defined by $X^{\delta-}$-$H^{\delta+}$···$H^{\delta-}$ -$Y^{\delta+}$, where Y is a transition metal. The electrostatic interaction between two hydrogens of opposite charge governs a dihydrogen bond. These two interactions represent two extreme cases of possible interactions between two hydrogen atoms [37].

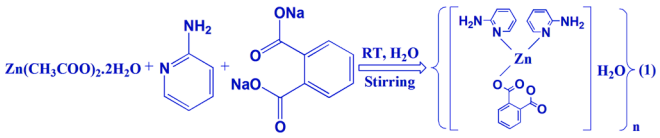

Scheme 2. Synthesis of **1**.

We have reported a number of novel coordination complexes with interesting architectures, stabilized by various unusual non-covalent interactions [38]. In continuation of our effort to synthesize and investigate coordination complexes with interesting supramolecular architectures; we, herein, present the synthesis, crystal structure, Hirshfeld surface analysis and theoretical study of a novel coordination polymer of Zn(II) with 2-aminopyridine (2-Ampy) and bridging *o*-phthalato (Phth) ligands viz. $\{[Zn(2\text{-Ampy})_2(Phth)]\bullet H_2O\}_n$ (**1**). Its crystal structure is mainly stabilized by C—H···H—C interactions. Considering the pharmacokinetic and toxicokinetic features, the polymer **1**-with zero Lipinski violations-may be a drug candidate. Its docking study with six important proteins of SARS-CoV-2 reveals good docking scores.The therapeutic potential of **1** was evaluated by ADMET calculations.

2. Experimental

2.1. Materials and methods

All reagents viz. zinc(II) acetate dihydrate, $Zn(CH_3COO)_2{\cdot}2H_2O$, 2-aminopyridine, *o*-phthalic acid and sodium hydroxide were obtained from Sigma Aldrich and Merk (India) ltd. All chemicals used were of analytical grade. They were used as received without further purification. The reaction was carried out in the deionized water medium. Elemental (C, H and N) analyses were carried out in a Perkin Elmer 2400 Series II CHNS/O analyzer. KBr phase FT-IR spectrum was recorded in a Shimadzu FTIR-8400S spectrophotometer in the mid-IR region (4000 to 600 cm^{-1}). The diffuse-reflectance UV-vis-spectra were recorded in a Shimadzu UV-2600 spectrophotometer. Thermogravimetric studies were carried out using a Mettler Toledo TGA/DSC1 STAR^e system at a heating rate of 10 °C min^{-1} under a flow of N_2 gas. The powder X-ray diffraction data were obtained using a XPERT-PRO X-ray powder diffractometer.

2.2. Synthesis of $\{[Zn(2\text{-Ampy})_2(Phth)]\bullet H_2O\}_n$ (1)

o-Phthalic acid (0.166 g,1.0 mmol) was dissolved in 20 ml of distilled water in a round-bottom flask containing NaOH (0.080 g, 2.0 mmol). An aqueous solution of $Zn(CH_3COO)_2{\cdot}2H_2O$ (0.219 g, 1.0 mmol) was added to the above solution. The solution was stirred at room temperature for about two hours. Now, 2-Ampy (0.188 g, 2.0 mmol) was slowly added to the resulting colorless solution. The whole solution was stirred for about another 4 h [Scheme 2]. The colorless solution was filtered and the filtrate was freezed. Colorless block-shaped crystals suitable for X-ray analysis were obtained from the filtrate after one week with a yield of 64.4 % based on $Zn(CH_3COO)_2{\cdot}2H_2O$. The crystals were filtered off, washed well with distilled water and dried in air. Anal. Calcd for $ZnC_{18}H_{18}N_4O_5$: C, 49.61; H, 4.16; N, 12.86. Found: C, 49.58; H, 4.13; N, 12.82. IR (KBr pellet, cm^{-1}): 3379 (m), 3217 (w), 3183 (w), 1663 (s), 1615 (s), 1589 (s), 1568 (s), 1379 (s), 765 (s), 657 (m).

2.3. X-ray crystallographic study

Molecular and crystal structures of **1** were determined by single crystal X-ray diffraction technique. Its intensity data was collected on a Bruker SMART APEX IICCD equipped with a graphite monochromatized Mo-Kα radiation (λ = 0.71073 Å) at 296 K. SAINT [39] was used for data

Table 1
Crystal data and structure refinement of **1**.

Crystal Data	{[Zn(2-Ampy)$_2$(Phth)]•H$_2$O}$_n$ (**1**)
CCDC Number	2166391
Empirical formula	$ZnC_{18}H_{18}N_4O_5$
Formula weight	435.73
Temperature (K)	293(2)
Wavelength (Å)	0.71073
Crystal system	Orthorhombic
Space group	*Pbca*
a (Å)	11.681(2)
b (Å)	17.594(4)
c (Å)	18.901(4)
α (°)	90.00
β (°)	90.00
γ (°)	90.00
Volume (Å^3)	3884.5(14)
Z	8
Calculated density (Mgm^{-3})	1.490
Absorption coefficient (mm^{-1})	1.301
F(000)	1792
Crystal size (mm^3)	29 × 21 × 16
θ range for data collection (°)	2.35 to 26.29
Index ranges	$-14\leq h\leq 14$, $-21\leq k\leq 21$, $-23\leq l\leq 23$
Reflections collected	113,215
Unique data[R_{int}]	3925 [0.0469]
Refinement method	Full-matrix least-squares on F^2
Data / restraints / parameters	3925 / 0 / 253
Goodness-of-fit on F^2	1.094
Final *R* indices[$I > 2\sigma(I)$] *R*1/ w*R*2	R1 = 0.0339, w*R*2 = 0.0787
R indices(all data) *R*1/ w*R*2	R1 = 0.0509, w*R*2 = 0.0921
Largest diff. peak and hole (e.Å^{-3})	0.346 and −0.310

integration. Intensities for absorption were corrected using SADABS [40]. The structure was solved by the direct method in the orthorhombic space group, *Pbca* with SHELXS-97 [41] and refined on F^2 using full matrix least squares techniques in the anisotropic approach for non-hydrogen atoms via WinGX [42]. The aromatic hydrogen atoms were placed at calculated positions and refined by standard procedures of SHELXL-97. The hydrogen atoms attached to water oxygen atoms were located in the difference Fourier maps and refined with isotropic displacement coefficients. The structural illustrations have been drawn using Diamond 3.0 [43]. Data collection and refinement parameters for **1** are summarized in Table 1.

2.4. Hirshfeld surface calculations

To check the contacts responsible for the stability of the crystal compound, Hirshfeld surface analysis was calculated with Explorer 17.5 associated with TONTO. 2D fingerprint plots of the compound were also computed using standard protocol [44].

2.5. Theoretical methods

The theoretical studies were conducted with density functional theory (DFT) using Gaussian14 to run the quantum chemical predictions [45]. The output files after normal termination were visualized in GaussView6.0. The hybrid functional method B3LYP and lanl2dz basis set were used during this study [46].

2.6. ADMET predictions

By determining the pharmacokinetic and toxicokinetic properties of drug candidate molecules early in the drug development process, additional experiments are not necessary, saving time and money and improving success rates. The absorption, distribution, metabolism, excretion, and toxicity (ADMET) factors specified the characteristics that a therapeutic molecule must have. The complex's absorption, distribution, metabolism, and excretion values were calculated using the Swiss ADME online database [47]. Toxicology values were computed

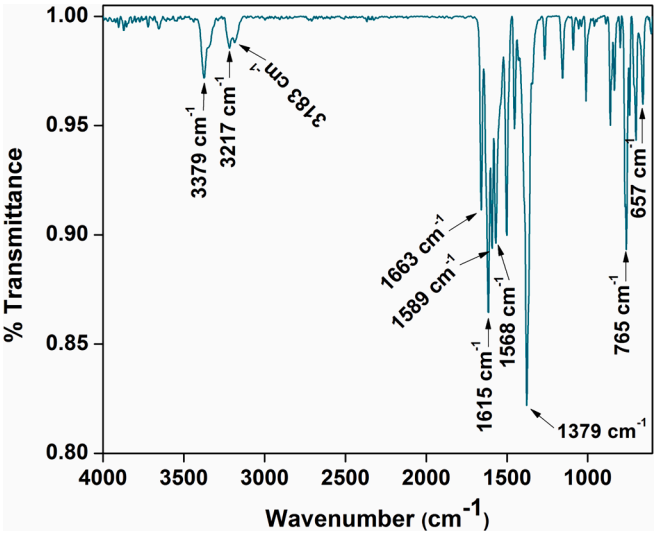

Fig. 1. FT-IR spectrum of **1**.

using the ProTox-II online database [48].

2.7. Docking studies

Molecular docking of the complex into the spike protein of Omicron variant (PDB Code: 7T9J) [49], main protease, M^{pro} (PDB Code: 7BQY) [50], NSP12 (PDB Code: 7BV2) [51], NSP15 (PDB Code: 6WXC) [52], NSP16 (PDB Code: 6WKQ) [53] and TMPRSS2 protease (PDB Code: 7MEQ) [54] was performed using AutoDock 4.2 [55]. The crystal structures of the spike protein of Omicron variant, main protease, NSP12, NSP15, and NSP16 and TMPRSS2 protease were taken from the RCS Protein Data Bank (https://www.rcsb.org./pdb). The Lamarckian Genetic Algorithm (LGA) technique was used for all calculations for the complex-target flexible docking. To provide the PDB format for the complex, to prepare the target from the structures of proteins, and to visualize the docking analysis were performed using DiscoveryStudio 4.0 [56].

3. Result and discussion

3.1. Synthesis and general aspects

The polymer{[Zn(2-Ampy)$_2$(Phth)]•H$_2$O}$_n$ (**1**) has been isolated in high yield by reacting one equivalent of zinc acetate dihydrate, Zn(CH$_3$COO)$_2$·2H$_2$O with two equivalents of 2-aminopyridine and one equivalent of disodium phthalate in water. The 1,6-bridging ability of the *o*-phthalato ligand imparts polymeric nature to **1**.The polymer is slightly soluble in water and its solubility in common organic solvents is also low. It shows a room temperature μ_{eff} value of 0.00 BM, thereby confirming the absence of unpaired electrons in its metal center.

3.2. Electronic spectroscopy

The electronic spectra of **1** were recorded in both solid and aqueous phases [Fig. S1]. For a Zn(II) ion, –a d^{10} system,–electronic transitions to the higher excited states are forbidden. So, in both the aqueous and solid phases, complex **1** does not show any spectral bands in the visible region. In the aqueous phase, the absorption band at 220 nm is attributed to the π–π* transition of the aromatic rings of 2-Ampy and the phthalato moieties. The other band at 269 nm is due to the n–π*transition. In the solid state UV-vis-NIR diffuse reflectance spectra, these bands of **1** get slightly shifted, – to 222 and 271 nm respectively. The appearance of the same bands of **1** at almost similar positions in both the phases suggests that the bonding modes and the geometry of complex **1** do not change

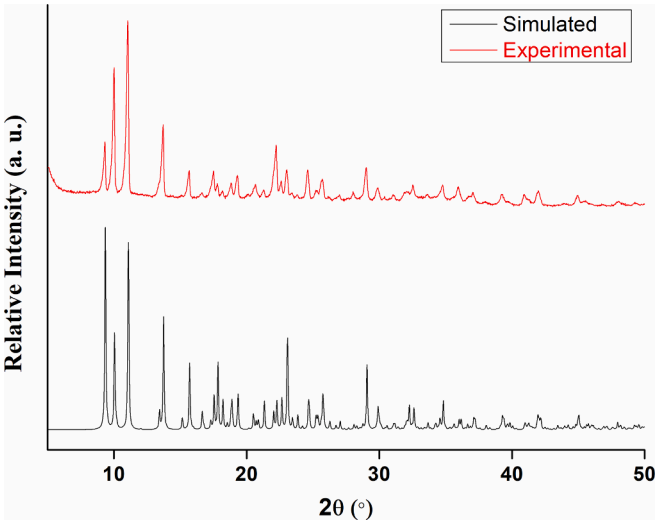

Fig. 2. Simulated and experimental PXRD patterns of **1**.

markedly in the aqueous phase [38].

3.3. IR spectrum

FT-IR spectrum of **1** (KBr pellets) was recorded in the region 4000–600 cm^{-1} [Fig. 1]. The bands are tentatively assigned based on earlier literature reports [57]. The absence of absorption bands in the range 1750–1670 cm^{-1} indicates that the $–COO^-$ groups in **1** remain completely de-protonated [58]. The broad absorption band at 3379 cm^{-1} is attributed to the ν(OH) vibrations of the lattice water molecule in the crystal. The absorption bands at 3217 and 3183 cm^{-1} are due to the ν(NH) vibrations of the coordinated 2-aminopyridine ligand. The carboxylate groups exhibit strong bands in the region 1690–1570 cm^{-1}. In **1**, these bands are shifted and broadened vis-à-vis the corresponding ones in the free phthalic acid. The present bands of the carboxylate, $–COO^-$ group are reflected by the asymmetric (ν_a) and symmetric (ν_s) stretching vibrations at 1663 and 1379 cm^{-1}, respectively. The difference between the asymmetric and symmetric stretches of the carboxylate groups [$\Delta = \nu_a – \nu_s = 284$ cm^{-1}] suggests their bridging binding mode to the metal ion. The strong absorption bands at 1615 cm^{-1} and 1589, 1568 cm^{-1} are attributed to the ν(C═N) and ν(C═C) vibrations in the ligands, respectively. The absorption bands at 765 and 657 cm^{-1} correspond to the ring-wagging vibrations of the pyridine groups in **1** [37,59]. These observations are in good agreement with the structure of **1** as determined by single-crystal XRD and elemental analyses.

3.4. Powder X-ray diffraction (PXRD)

The phase purity of the complex **1** was studied by powder X-ray diffraction (PXRD) experiment. As shown in Fig. 2, the experimental patterns are in good agreement with the simulated ones obtained from the single crystal X-ray diffraction data, suggesting that the synthesized crystals of **1** are true representatives of its bulk material. Differences in intensity between the experimental and simulated patterns may be attributed to the preferential orientations of the crystalline powders.

3.5. Crystal structure

The details of single crystal XRD and structure refinement data of polymer **1** are presented in Table 1. It crystallizes in the orthorhombic space group *Pbca*. The polymeric unit is shown in Fig. 3, together with the atomic numbering scheme. The crystal structure of the polymer **1** contains a basic trimeric unit $[Zn_3L_6Ĺ_4]•H_2O$ (where L = 2-Ampy and Ĺ = Phth) with the same Zn···Zn distances of 5.87 Å. It basically consists of $[Zn(2\text{-Ampy})_2]$ entities linked together by bridging *o*-phthalate anions in the μ_2-1,6 coordination mode, thereby forming a metal-binding site of N_2O_2 type around each of the Zn(II) centers. Each Zn(II) ion, thus, possesses a distorted tetrahedral coordination sphere built by the *o*-phthalate oxygens (O2 and O4) and 2-aminopyridine nitrogens (N1 and N3). The coordination angles about Zn centers are in the range 101.47 (8) – 107.77(8)° except for O2 – Zn1 – N3 of 128.13(9)°. The distortion of the tetrahedron around each Zn(II) ion can be indicated by the value of τ_4 – a parameter introduced by Houser [60] to describe the geometry of a four coordinate complex. For **1**, the value of τ_4 is 0.88 (for an ideal tetrahedron, $\tau_4 = 1$). The distorted tetrahedral geometry at each Zn(II) center in **1** can partly be attributed to the spatial orientation of the bridging ligands. The planes through the carboxylate groups O4-C7-O5 and O2-C1-O3 of the bridging *o*-phthalato ligand make dihedral angles of 27.21(3) and 66.24(2)° respectively with the aromatic ring.The selected bond lengths (Å) and bond angles (°) of **1** are presented in Table 2. These values are comparable with those in similar compounds in literature [61].

The solid state structure of polymer **1** shows a combination of

Table 2
Selected bond lengths (Å) and bond angles (°) of **1**.

Bond	d (Å)	Angle	θ(°)
Zn1-O2	1.949(3)	O2-Zn1-O4	101.47(8)
Zn1-O4	1.974(2)	O2-Zn1-N1	106.99(8)
Zn1-N1	2.047(2)	O2-Zn1-N3	128.13(9)
Zn1-N3	2.021(3)	O4-Zn1-N1	104.53(8)
		O4-Zn1-N3	105.60(8)
		N1-Zn1-N3	107.77(8)

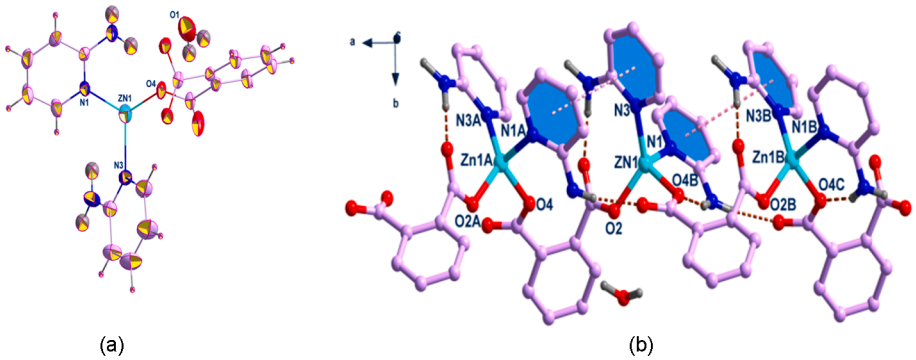

Fig. 3. (a) ORTEP diagram of **1** with the partial atomic labeling scheme, showing 30 % probability ellipsoids. (b) View of the coordination environment of Zn atoms in the π···π interactions stabilized basic trimeric unit of **1**. Irrelevant hydrogen atoms are omitted for clarity. Symmetry codes: A. 0.5 + x, y, 0.5 – z; B. – 0.5 + x, y, 0.5 – z; C. – 1 + x, y, z.

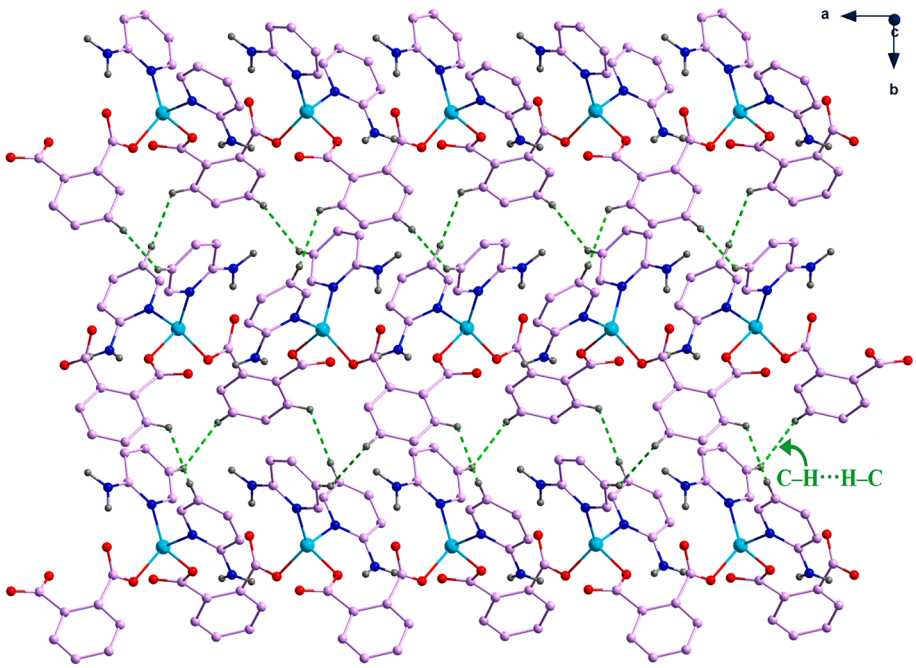

Fig. 4. The layered structure of **1** in the *ab*-plane through C—H···H—C interactions. Interactions between neighboring polymeric chains are only shown. Irrelevant H-atoms are omitted for clarity.

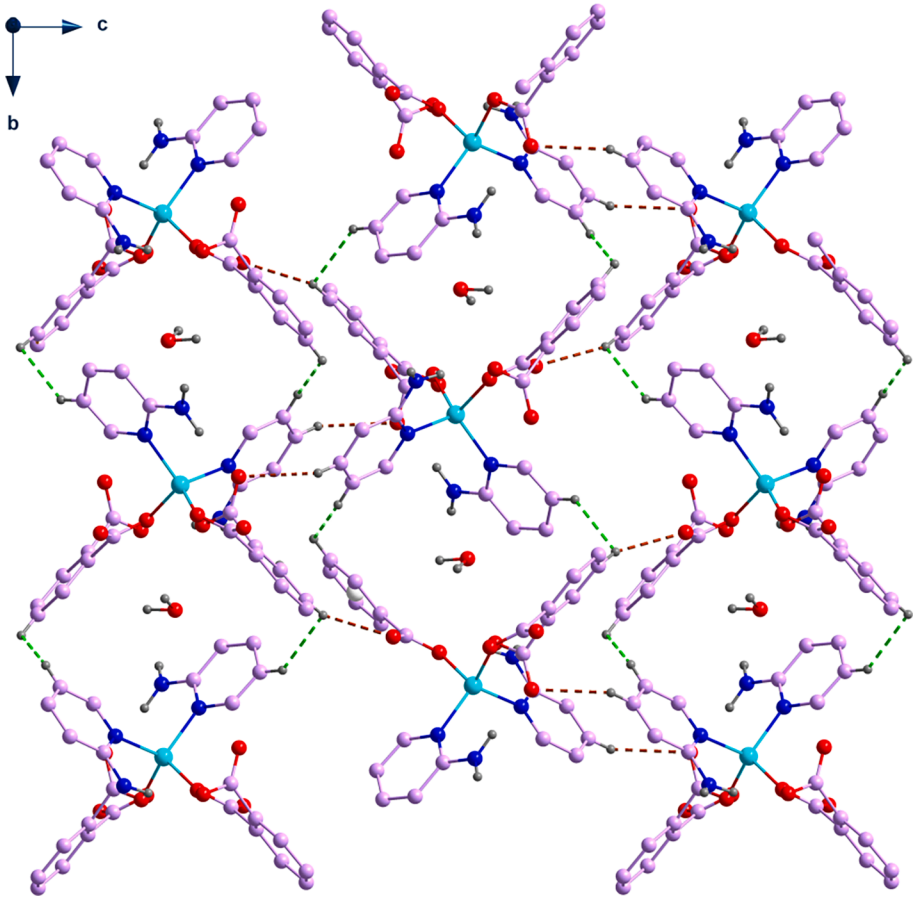

Fig. 5. Stacking of **1** along the crystallographic *c*-direction via C—H···O and C—H···H—C interactions. Irrelevant H-atoms are omitted for clarity.

N—H···O and π···π interactions. The bridging nature of the *o*-phthalato carboxylate group linking the Zn1 atom to its neighbors Zn1A atom (0.5 + x, y, 0.5 − z) and Zn1B atom (−0.5 + x, y, 0.5 − z) makes the trinuclear $[Zn_3(2\text{-Ampy})_6(Phth)_4]\bullet H_2O$ core. As shown in Fig. 3, the trimeric unit of **1** is stabilized by N—H···O and π··· π interactions. The amino N2 atom of the coordinated terminal 2-aminopyridine ligand acts

Table 3
Hydrogen bonding parameters (Å and °) for **1**.

D–H···A	d(D–H)	d(D–A)	d(H···A)	<(DHA)
N2–H2A···O5[a]	0.850	2.885	2.047(4)	168.81(16)
N2–H2B···O4[b]	0.903	2.840	1.977(3)	159.63(15)
N4–H4A···O3	0.956	2.888	1.935(3)	173.86(16)
C3–H3···O5[c]	0.903	3.595	2.714(4)	158.42(14)
C15–H15···O3[d]	0.930	3.346	2.569(6)	141.30(14)

Symmetry codes: a: x–1,+y,+z; b: x–1/2, +y, –z + 1/2; c: x–1/2, –y + 1/2, –z; d: –x + 1, –y, –z.

Table 4
Intermolecular C—H···H—C interactions (Å and °) for **1**.

C—H···H—C	d(C—H)	d(H···H)	<(C—H···H)	<(H···H—C)
C3–H3···H9–C9	0.93/0.93	2.60	112.26	140.02
C4–H4···H16–C16	0.93/0.93	2.63	114.76	141.54
C5–H5···H16–C16	0.93/0.93	2.44	122.73	136.84

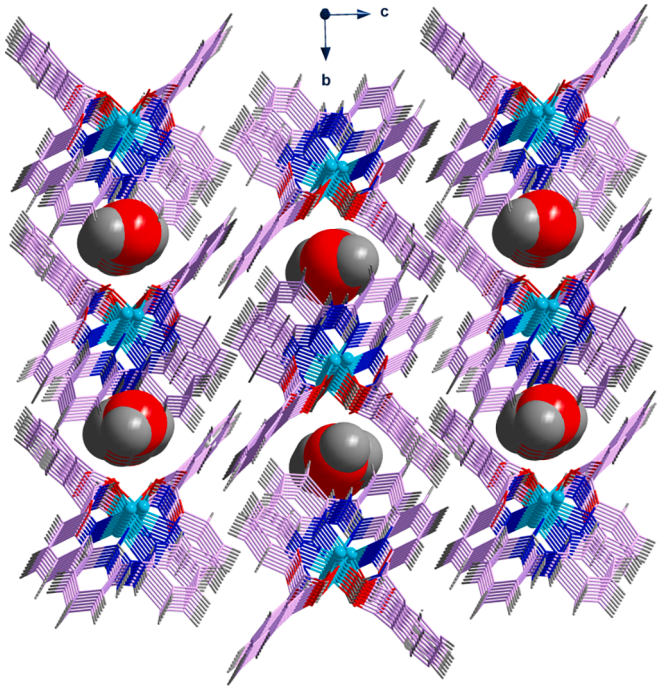

Fig. 6. View of lattice water enclathrated 3D architecture of **1** along *a*-direction.

as a donor to the coordinated and uncoordinated carboxylate oxygen atoms, O4 and O5 from two coordinated *o*-phthalato ligands to form N2−H2B···O4 and N2−H2A···O5 hydrogen bonds at a donor–acceptor distance of 2.84 and 2.86 Å, respectively. Similarly, the uncoordinated carboxylate oxygen atom O3 of the coordinated *o*-phthalato ligand is a hydrogen bond acceptor, forming interactions with the amino (N4) group of the other coordinated 2-aminopyridine ligand. This hydrogen-bonding interaction is almost linear with the angle at the H of 173.86° and N4−H2A···O3 distance of 1.94 Å. Additional reinforcement to the basic trimeric unit of **1** is provided by π···π interactions with the pyridyl rings of the two coordinated terminal 2-aminopyridine ligands overlapping with each other at a centroid-to-centroid separation of 3.92 Å.

In the crystal structure of **1**, the trinuclear units {Zn_3(2-Ampy)$_6$(Phth)$_4$} are interconnected through the bridging phthalato ligands, thereby forming a polymeric linear 1D chain that extends along the crystallographic *a*-direction. These polymeric chains get interconnected through two types of C—H···H—C interactions. The C3–H3

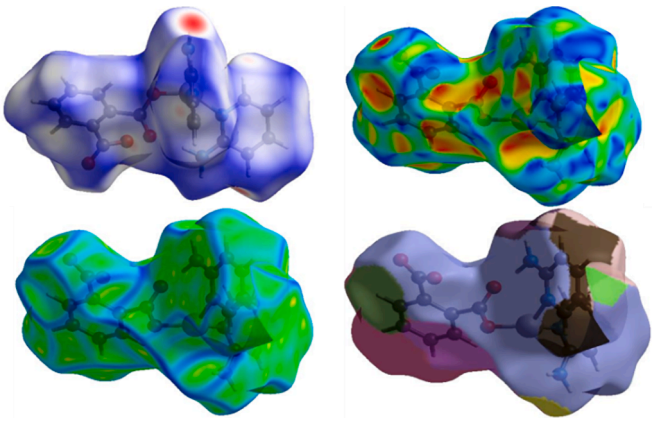

Fig. 7. Hirshfeld surface analysis of **1**.

moiety of the bridging phthalato ligand in one polymeric chain is involved in C—H···H—**C** interaction with the C9–H9 moiety of the coordinated 2-aminopyridine ligand from a neighboring chain. Similarly, the C5–H5 moiety from the same phthalato ligand and 2-aminopyridine ligand from the same neighboring polymeric chain (but coordinated to a different Zn(II) center) interacts through another C—H···H—**C** interaction involving C5–H5 and C16–H16 moieties. This results in a layered structure of **1** in the *ab*-plane [Fig. 4].

These layers of **1** in the *ab*-plane are stacked together along the crystallographic *c*-direction via C—H···O and C—H···H—C interactions [Fig. 5]. Two types of C—H···O interactions contribute to such stacking. The first involves C15–H15···O5 hydrogen bond between the coordinated phthalato and 2-aminopyridine ligands from two neighboring Zn (II) centers at a.

H···O distance of 2.57 Å [Table 3]. The other utilizes atom O5 as the acceptor and C3 as the donor with a donor–acceptor distance of 3.59 Å. Final reinforcement to this staking is provided by other two C—H···H—**C** interactions involving C3–H5, C9–H9 and C4–H4, C16–H16 moieties [Table 4]. One interesting feature of this stacking is the enclathration of the lattice water molecules. This kind of formation of a layered structure in a plane and the stacking thereof along a direction perpendicular to it gives rise to a 3D architecture of **1** [Fig. 6].

3.6. *Hirshfeld surface analysis*

The whole electron density of a molecule in the crystal lattice can be divided into various fragments based on the electron density with the help of Hirshfeld surface analysis [62]. This tool can be used to check the quantity of the nature of the interactions known as intermolecular interactions. The HS analysis was carried out according to the reported method cited in the experimental section using CrystalExplorer17. The HS was computed over d_{norm} range of −0.55 to 1.0 Å, the curvedness range of −0.40 to 4.0 Å and the shape index range of −0.10 to 1.0 Å. The surfaces appeared transparent to display the visualization of the molecules, over which they were mapped [Fig. 7].The different color schemes such as red, white and blue showed intermolecular connections with distances less than, identical to, and higher than van der Waals radii, respectively [63]. On the surface, the dark red coloration occurred about the nitrogen atom of amino group and pyridine ring along with the oxygen atom of carbonyl groups. These areas indicated the donor positions for the neighboring atoms and showed hydrogen bonding with other atoms. Bright red areas showed the intermolecular contacts less than their *vdW* radii and the blue spots showed intermolecular contacts longer than their *vdW* radii, while white spots denoted the total sum of their radii (*vdW*).

Likewise, 2D (two-dimensional) finger print (FP) plots were plotted to obtain quantitative information regarding the nature and the kind of intermolecular contacts exerted by the molecule in the crystal packing

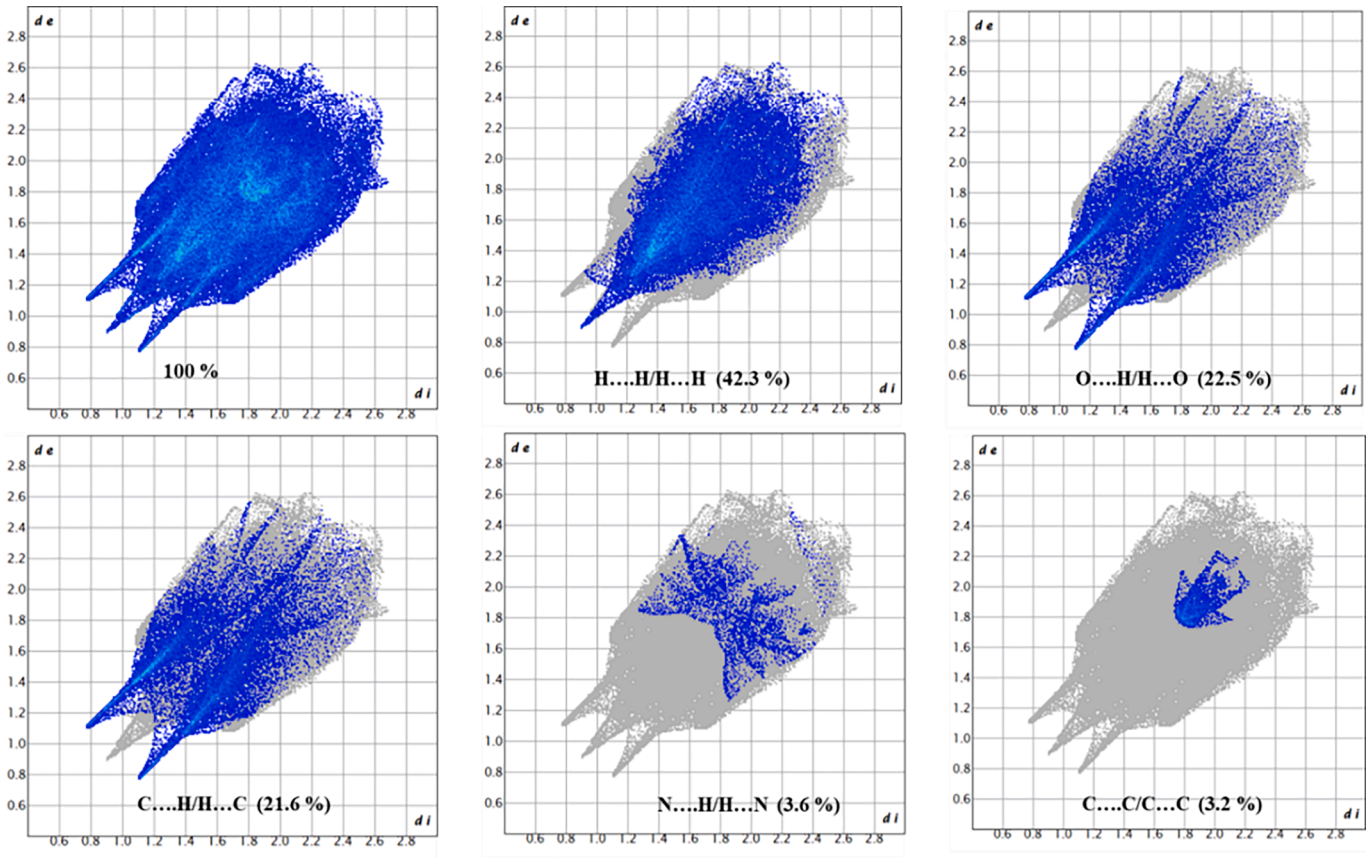

Fig. 8. Fingerprint plots of contacts along with their relative contributions for **1**.

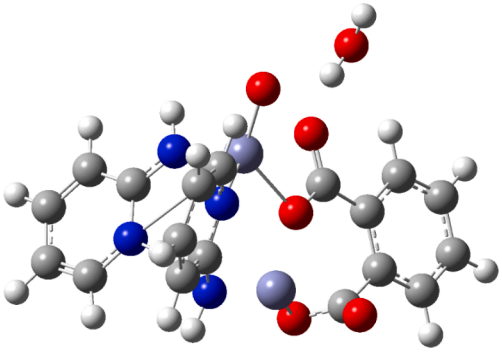

Fig. 9. DFT energy minimized structure of **1**.

[64]. The finger print plots were figured into every interatomic contact and for the whole interactions. The reciprocal contact for every inter-atomic contact was calculated for the specific inter-atomic contacts [Fig. 8]. The spikes represented the inter-atomic contacts that have major contributions in the crystal packing of the molecule. The inter-atomic contacts which have an excellent impact on the crystal packing of the molecule as compared to the others were H···H, O···H and C···H with percentage (%) contributions of 42.3 %, 22.5 %, and 21.6 %, respectively as shown in Fig. 8. The N···H (3.6 %) and C···C (3.2 %) depicted less contribution to crystal packing as compared to others.

It has been seen in the Hirshfeld analysis or topographical surface analysis that H···H interactions are present in the crystal structure of **1**, which can be seen in XRD analysis also. In 2D fingerprint plot, the major contribution in the structure is due to H···H interactions. Furthermore, the H···H interactions were drawn throughout the understudied molecule. The distance of the H···H interaction were measured in the crystal structure and it was found that these interactions are present between hydrogen atom of the amino group with phenyl hydrogen with different distances as shown in Fig. S2 (a-d). The distance is 5.80 Å, 5.56 Å, 7.17 Å and 4.92 Å as shown in Fig. S2b, while it is 3.03 Å, 3.74 Å, 7.39 and 5.56 Å in Fig. S2c. Similarly, H···H interactions are 3.12 Å, 4.92 Å, 2.91 Å and 5.59 Å in Fig. S2d.

3.7. Optimized molecular geometry

The targeted molecule was optimized with Gaussian 16 software using B3LYP (hybrid functional) method and lanl2dz basis set. The optimized structure of the under studied compound was shown in Fig. 9. The comparative study of the optimized bond length and bond angles was also carried out with the experimental values obtained from XRD technique. It was observed that the theoretical bond length and bond angles deviated to some extent from the crystal parameters. This is due to the phase difference involved in the two calculations: in DFT, calculations were made in the gaseous phase, whereas experimental measurements were done in the solid crystalline state. The Zn1-N1 and Zn1-N2 bond lengths were 2.047 and 2.021 Å, while these values were 3.571 and 2.191 Å in experimental calculations, respectively. Zn1-O4 was 1.974 Å in XRD while it was 1.890 Å in DFT; similarly Zn1-O2 was 1.949 and 2.134 Å in XRD and DFT, respectively. The O2-Zn1-O4 bond angle was 101.47° in XRD, while it was 129.21° in DFT and O2-Zn1-N1 in XRD was 106.99° while it was 95.93° in DFT. In the solid state of **1**, the bond angles O2-Zn1-N3, O4-Zn1-N1, O4-Zn1-N3 and N1-Zn1-N3 were 128.13°, 104.53°, 105.60° and 107.77° respectively. DFT calculations showed these bond angles to be 144.905°, 98.219°, 85.881° and 76.060° respectively. Furthermore, the observed deviation might be because the XRD structure was resolved in the crystalline system, while the calculations for the optimized structures in the form of DFT studies were for the isolated molecule [65].

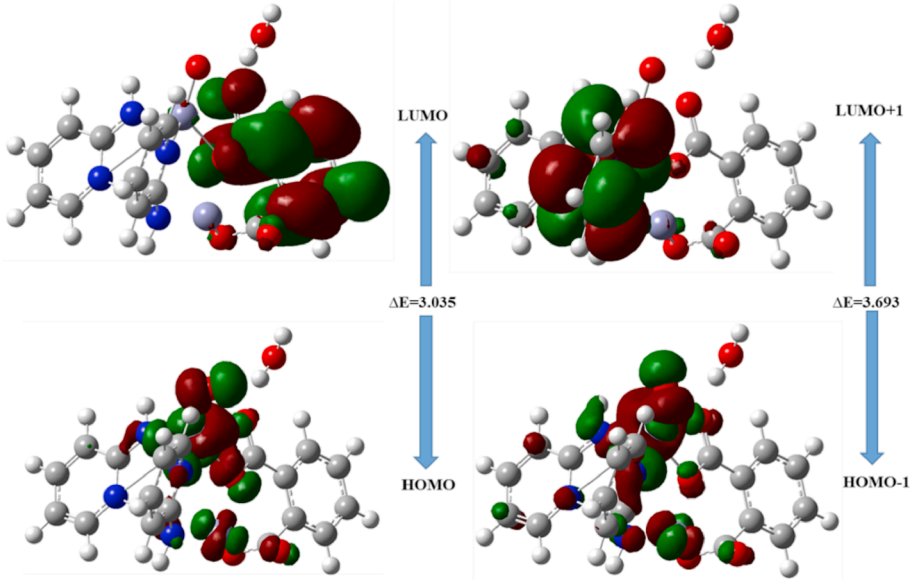

Fig. 10. Energy gap measurement (HOMO − LUMO and HOMO − 1 − LUMO + 1) of **1**.

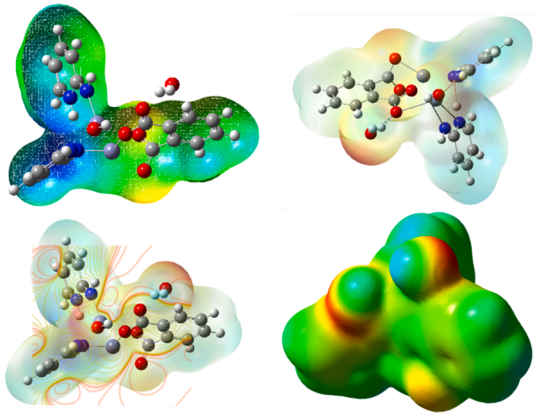

Fig. 11. Molecular electrostatic potential of **1**.

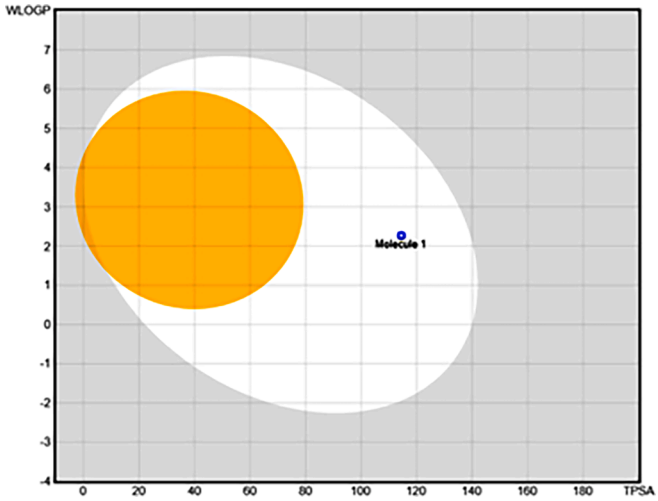

Fig. 12. BOILED-Egg model of polymer **1**.

The DFT calculations in terms of HOMO and LUMO energy gap were also calculated and it was found that the energy gap between HOMO and LUMO was 3.035 eV while HOMO − 1 and LUMO + 1 energy gap was 3.693 eV. These values predicted that the synthesized compound was highly stable in nature. The calculated HOMO and LUMO orbitals are shown in Fig. 10 along with the energy gaps. The charge on each atom in the molecule significantly affects the properties of the molecule. This also affects the magnitude of the dipole moment, electronic dispersion, acidity/basicity behavior, and vibration modes. Furthermore, the charge distribution on the molecule is used to differentiate its donor atoms from the acceptor ligand atoms. Molecular electrostatic potential (MEP) was also mapped with DFT studies [Fig. 11]. It also offers information regarding the reactive spots, molecular size and shape on the surface of the molecule. The surface displayed different color schemes: red depicted the electron-rich area with a fractional negative charge and blue, an electron-deficient area with a partial positive charge, light blue depicted slightly electron-deficient region, yellow represented slightly electron-rich region and green showed a neutral region [66].

3.8. Evaluation of drug-likeness and toxicological properties

Predicting the pharmacokinetic and toxicokinetic properties of therapeutic candidate molecules increases the likelihood of successful drug development. Lipinski and coworkers reported five rules for assessing whether a chemical is a drug candidate [67]. When the findings were evaluated, it was determined that polymer **1** complied with Lipinski's five rules [Table 4]. BOILED-Egg model of polymer **1** showed that its gastrointestinal absorption is high, it cannot cross the blood–brain barrier (BBB), and it can be used as substrates of P-glycoprotein [Fig. 12]. The compound's solubility in octanol/water is found as low. According to the predicted findings, the complex does not interact with cytochrome P450 enzymes (CYPs) CYP2C19, CYP2C9, CYP1A2, CYP2D6, and CYP3A4. Polymer **1** is active in hepatotoxicity, but it is inactive in carcinogenicity, immunotoxicity, mutagenicity, cytotoxicity, and mitochondrial membrane potential (MMP). When all these advantages and disadvantages are evaluated, it is suggested that the complex can be a candidate drug and drug formulation studies may be pursued.

3.9. Docking studies

The disease COVID-19, which developed in late 2019 with the emergence of a new coronavirus named SARS-CoV-2, caused a global pandemic. The effects of the coronavirus disease continue. Drug studies

Table 5
The pharmacokinetic properties of polymer **1**.

Properties	Predicted Result
Molecular weight[a]	483.10
Number of heavy atoms	28
Number of aromatic heavy atoms	18
Number of rotatable bonds	7
Number of H-bond acceptors	4
Number of H-bond donors	2
Molar Refractivity	94.56
TPSA (Å^2)	114.50
Log $P_{o/w}$	2.27
GI absorption	High
BBB permeant	No
P-gp substrate	Yes
CYP1A2 inhibitor	No
CYP2C19 inhibitor	No
CYP2C9 inhibitor	No
CYP2D6 inhibitor	No
CYP3A4 inhibitor	No
LogK_p (skin permeation)	–7.08
Lipinski	Yes; 0 violation
Toxicity class[b]	5
Predicted LD_{50}	2850 mg/kg
Hepatotoxicity	Active
Carcinogenicity	Inactive
Immunotoxicity	Inactive
Mutagenicity	Inactive
Cytotoxicity	Inactive
MMP[c]	Inactive

[a]Molecular weight unit g/mol
[b]Toxicity class1-toxic; 6-non-toxic
[c]MMP: Mitochondrial membrane potential

for the treatment of the disease are still ongoing. For this purpose, to investigate the binding interaction of the complex, the molecular docking of polymer **1** has been performed on six important proteins of SARS-CoV-2 (spike protein of Omicron variant, main protease (M^{pro}), NSP12, NSP15, NSP16 and TMPRSS2 protease).

According to the calculated results, the binding scores for polymer **1** with spike protein of Omicron variant, main protease (M^{pro}), NSP12, NSP15, NSP16 and TMPRSS2 protease were determined to be –5.9, –8.1, –5.5, –7.7, –7.4 and –6.4 kcal/mol, respectively. Interestingly enough, these scores (for spike protein and main protease, M^{pro}) are better than the corresponding scores for chloroquine, hydroxychloroquine and remdesivir [68].

Polymer **1** exhibits the hydrogen bond with amino acids such as Asp867 and His1058, carbon-hydrogen interaction with His1058, metal-acceptor interaction with Met731, π-anion interaction with Aps867, π-sigma interaction with Val860, π-alkyl with Pro863 and Pro1057 in the spike protein of Omicron variant [Table 5]. The distances of hydrogen bonds of polymer **1** with the Asp867 and His1058 amino acid residues of the spike protein of Omicron variant were found as 2.94 Å and 2.05 Å, respectively [Fig. 13]. It exhibits attractive charge interaction with His41, hydrogen bonds with Gln189, His41, Cys145, π-anion interaction with His41, π-alkyl interactions (Table 6) with Met165 and Cys145, metal interaction with Cys145 residue in the active site of main protease, M^{pro} of SARS-CoV-2. The hydrogen bond distances of polymer **1** with the Gln189, His41, and Cys145 amino acid residues of main protease enzyme were found as 2.65 Å, 2.74 Å and 3.75 Å, respectively [Fig. 14]. It showed attractive charges interactions with Agr555, hydrogen bonds with Agr555 (at 2.39 Å), Asn691 (at 2.81 Å), and Ser759 (at 2.24 Å), π-anion interactions with Asp760, π-sulfur interactions with Cys622 and π-alkyl interaction with Ala688 of NSP12 protein of SARS-CoV-2 [Fig. 15]. Polymer **1** interacts with salt bridge with Lys290 residue, attractive charge with His235 and His250, hydrogen bonds with His250 (at 2.10 Å), Thr341 (at 2.29 Å) and Tyr343 (at 2.97 Å), metal-acceptor with Gln245, π-donor hydrogen bond with Trp333, π-sigma with Tyr341, π-π stacking with Tyr343 and π-π T shaped with Trp333 of NSP15 protein of SARS-CoV-2 [Fig. 16]. Polymer **1**

Table 6
Binding energy and interactions of **1** with SARS-CoV-2.

Protein	Binding energy (kcalmol^{-1})	Active site residues involved in interactions
Spike protein	–5.9	Asp867, His1058, Met731, Val860, Pro863, Pro1057.
M^{pro}	–8.1	His41, Gln189, Cys145, Met165.
NSP12	–5.5	Agr555, Asn691, Ser759, Asp760, Cys622, Ala688.
NSP15	–7.7	Lys290, His235, His250, Thr341, Tyr343, Gln245, Trp333, Tyr341.
NSP16	–7.4	Lys6968, Lys6844, Asn6928, Asp6928, Asp6897, Pro6932.
TMPRSS2 protease	–6.4	His334, Val479, His41, Asp482, Asp482, Arg150, Pro369, Met478, Val479.

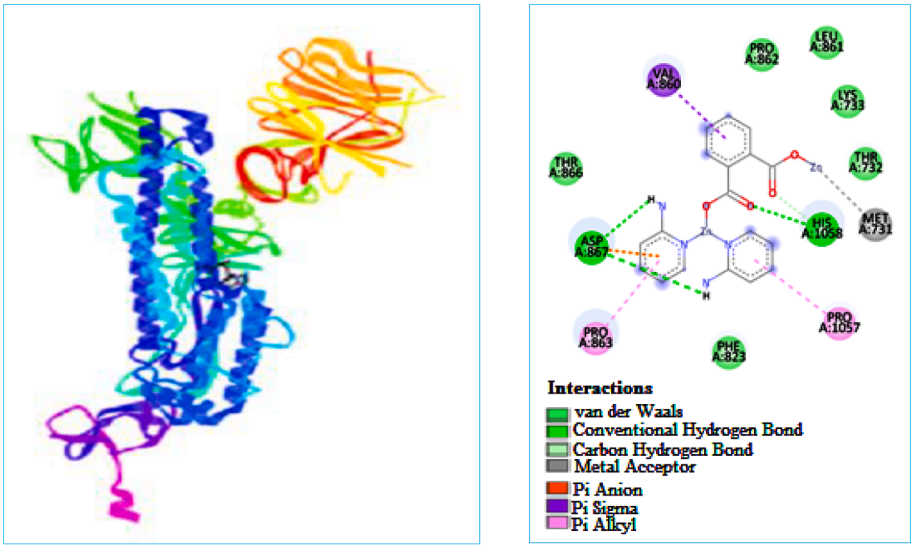

(a) (b)

Fig. 13. The molecular docking results of polymer **1** on the spike protein of Omicron variant of SARS-CoV-2 (a), 2D interactions of polymer **1** with amino acids in the active site of the spike protein of Omicron variant of SARS-CoV-2 (b).

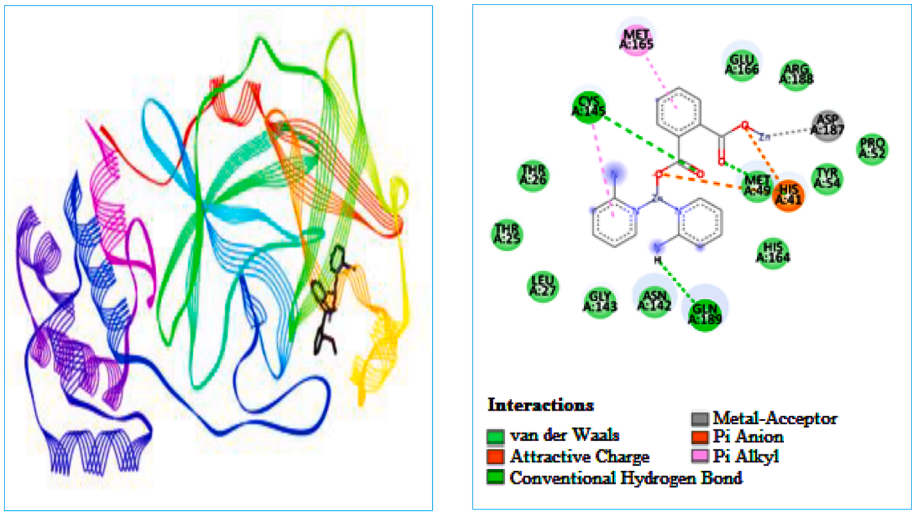

Fig. 14. The molecular docking results of polymer **1** on the main protease enzyme, M^{pro} of SARS-CoV-2 (a), 2D interactions of polymer **1** with amino acids in the active site of main protease enzyme, M^{pro} of SARS-CoV-2 (b).

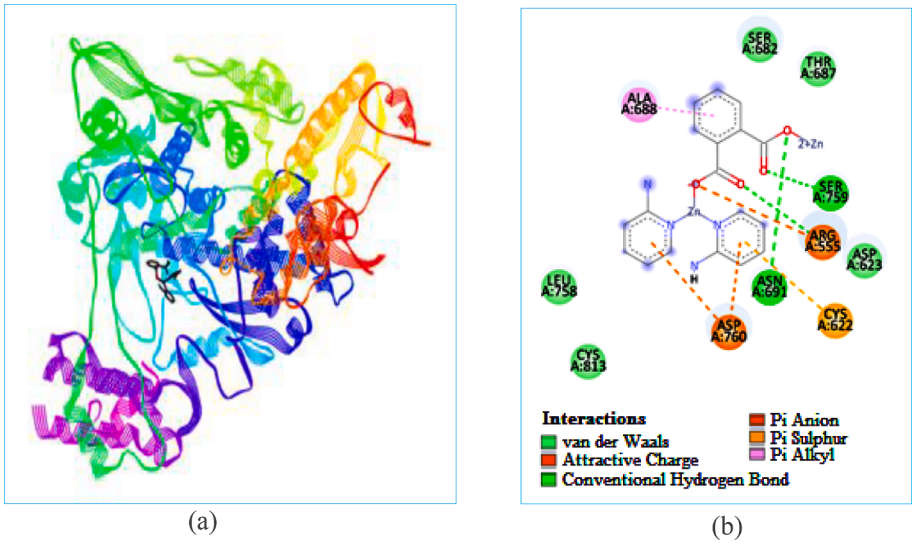

Fig. 15. The molecular docking results of polymer **1** on the NSP12 protein of SARS-CoV-2 (a), 2D interactions of polymer **1** with amino acids in the active site of NSP12 of SARS-CoV-2 (b).

makes salt bridge with Lys6968 residue, attractive charge with Lys6844, hydrogen bonds with Asn6928 (at 2.97 Å) and Lys6844 (at 2.39 Å), metal-acceptor with Asp6928, π-anion with Asp6897, π-alkyl with Pro6932 of NSP16 protein of SARS-CoV-2 [Fig. 17]. Polymer **1** also binds via attractive charge interaction with His334, hydrogen bond with Val479, π-anion interaction with His41, π-anion interactions with Asp482, π-sigma with Asp482, π-alkyl interactions with Arg150, Pro369, Met478 and Val479 residues in the active site of TMPRSS2 proteases of SARS-CoV-2 [Fig. 18]. The hydrogen bond distance of polymer **1** with the Val479 residue of TMPRSS2 proteases was found as 2.41 Å. When all the results obtained were evaluated, it was found that polymer **1** makes many important electrostatic and hydrophobic interactions as well as strong hydrogen bond interactions with the important targets of SARS-CoV-2. Therefore, further *in vitro/in vivo* studies of polymer **1** are recommended.

3.10. Thermal analysis

The thermal behavior of **1** was investigated by the use of TGA and DSC. The TGA curve of **1** shows a multistep decomposition [Fig. S3]. The first 5.13 % weight loss (calculated 4.13 %) occurs in a single-step loss (please see DSC) between 40 and 110 ℃ and is due to the loss of the lattice water molecule per formula unit. The second weight loss (35.74 %) from 130 to 237 ℃ is attributed to the partial breakdown of the framework caused by the loss of the phthalato ligand (calculated 37.66 %). The last decomposition (41.58 %) can be attributed to the loss of the two coordinated 2-aminopyridine ligands (calculated 43.20 %). This occurs in three interconnected steps between 252 and 800 ℃ (please see DSC).The final weight at 800 ℃ is approximately 20.38 % suggesting the predominance of ZnO (calculated 18.68 %).

The DSC thermogram shows four exothermic and one endothermic peaks [Fig. S3 (inset)]. The first exothermic peak (98 ℃) corresponds to desolvation of the polymer. The endothermic peak (194 ℃) signifies the loss of the phthalato ligand. The last exothermic peaks (340, 372, 437

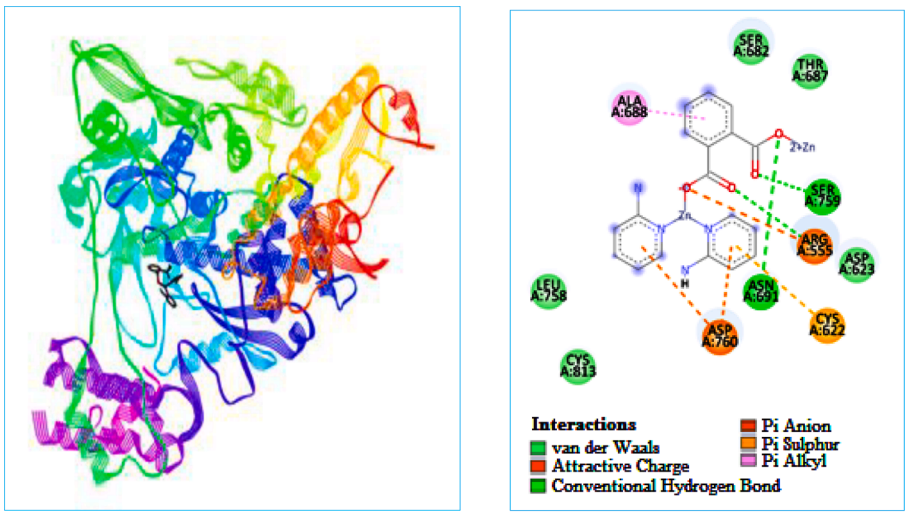

(a) (b)

Fig. 16. The molecular docking results of polymer **1** on the NSP15 protein of SARS-CoV-2 (a), 2D interactions of polymer **1** with amino acids in the active site of NSP15 of SARS-CoV-2 (b).

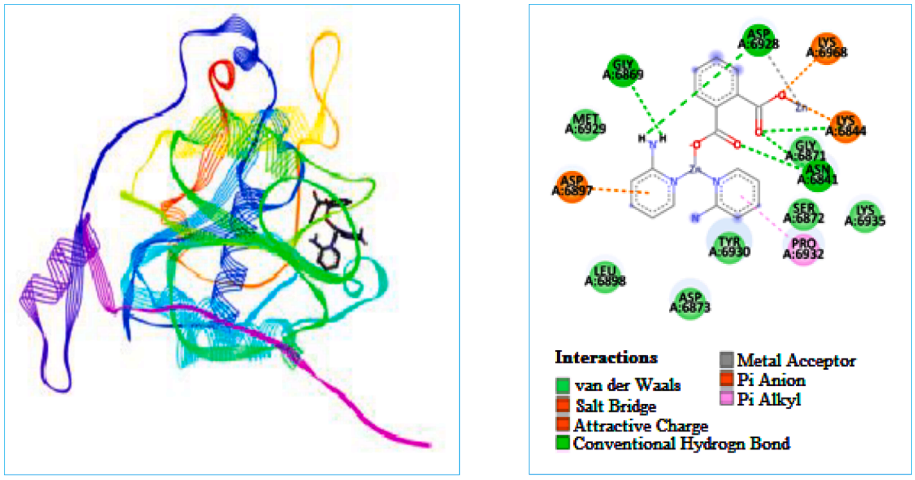

(a) (b)

Fig. 17. The molecular docking results of polymer **1** on the NSP16 protein of SARS-CoV-2 (a), 2D interactions of polymer **1** with amino acids in the active site of NSP16 of SARS-CoV-2 (b).

and 460 ℃) represent the loss of the two coordinated 2-aminopyridine ligands [69].

4. Conclusion

A novel supramolecular coordination polymer, {[Zn(2-Ampy)$_2$(Phth)]•(H_2O)]}$_n$ (**1**) of Zn(II) involving bridging *o*-phthalato ligand has been synthesized and characterized by single crystal X-ray diffraction, elctronic spectroscopy, FT-IR, PXRD and thermal analysis. In the crystalline state, the polymer **1** has a basic trimeric unit that is stabilized by N—H···O and π···π interactions. The bridging phthalato ligands interconnect these trinuclear units to form a polymeric 1D chain, which get interconnected through C—H···H—C interactions to give a layered architecture of **1** in the *ab*-plane. These layers stack together along the *c*-direction through C—H···O and C—H···H—C interactions, thereby resulting in a 3D structure with the lattice water molecules enclathrated therein. DFT results showed a good coherence between the values from experimental and computational studies. Various contacts of the polymer were checked by Hirshfeld surface analysis, which revealed that the H···H interactions were the foremost contributors to its stabilization. The *in silico* inhibitory action of the compound was studied by molecular modeling study with six important proteins of SARS-CoV-2 viz. spike protein of Omicron variant, (PDB Code: 7T9J), main protease, M^{pro} (PDB Code: 7BQY), NSP12 (PDB Code: 7BV2), NSP15 (PDB Code: 6WXC), NSP16 (PDB Code: 6WKQ) and TMPRSS2 protease (PDB Code: 7MEQ). 2D and 3D molecule-enzyme contacts and their docking positions proposed that the synthesized compound is a good inhibitor against them. The docking scores with spike protein and M^{pro} are even better than the common antiviral drugs against SARS-CoV-2. Its ADMET study revealed satisfactory pharmacokinetic and toxicokinetic properties. The experimental and computational investigations recommended that *in vivo* and supplementary studies might be pursued for the validation of the polymer **1** in the therapeutic field.

CRediT authorship contribution statement

Swah Mohd. Nashre-ul-Islam: Conceptualization, Software, Writing – original draft, Writing – review & editing. **Kamala Kanta**

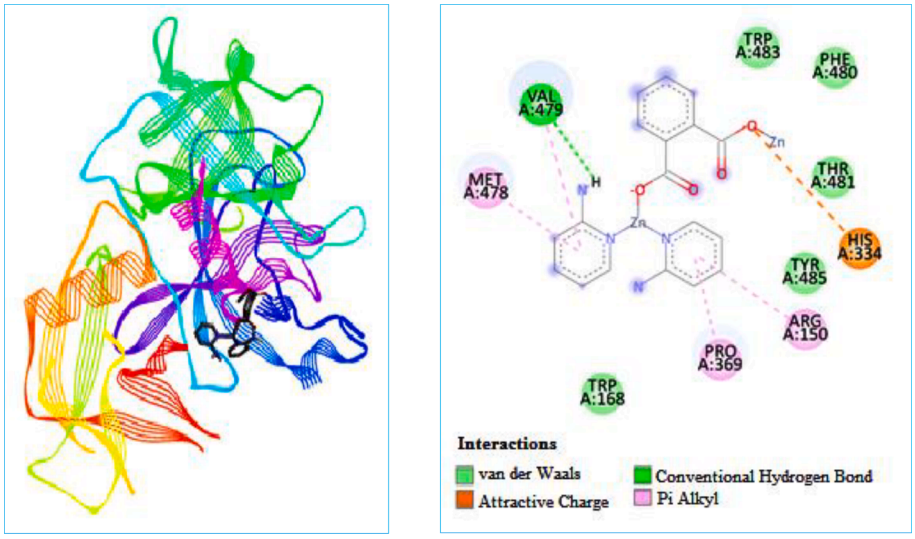

(a) (b)

Fig. 18. The molecular docking results of polymer **1** on the TMPRSS2 protease of SARS-CoV-2 (a), 2D interactions of polymer **1** with amino acids in the active site of NSP15 of SARS-CoV-2 (b).

Borah: Writing – review & editing. **Muhammad Asam Raza:** Software, Writing – original draft. **Füreya Elif Öztürkkan:** Software, Writing – original draft.

Declaration of Competing Interest

The authors declare that they have no known competing financial interests or personal relationships that could have appeared to influence the work reported in this paper.

Data availability

Data will be made available on request.

Acknowledgement

SMNI and KKB thankfully acknowledge Dr. Babita Sarmah, Associate Professor, Mangaldai College, India for her moral support and encouragement in completion of the manuscript.

Appendix A. Supplementary data

Supplementary data to this article can be found online at https://doi.org/10.1016/j.poly.2023.116304.

References

[1] R.C. Burrows, J.C. Bailar Jr., J. Inorg. Nucl. Chem. 29 (1967) 709–714, https://doi.org/10.1016/0022-1902(67)80327-0.
[2] T.-L. Easun, F. Moreau, Y. Yan, S. Yang, M. Schröder, Chem. Soc. Rev. 46 (2017) 239–274, https://doi.org/10.1039/C6CS00603E.
[3] M. O'Keeffe, O.M. Yaghi, Chem. Rev. 112 (2012) 675–702, https://doi.org/10.1021/cr200205j.
[4] D. Zhao, D.J. Timmons, D. Yuan, H.-C. Zhou, Acc. Chem. Res. 44 (2011) 123–133, https://doi.org/10.1021/ar100112y.
[5] R.A. Agarwal, N.K. Gupta, Coord. Chem. Rev. 332 (2017) 100–121, https://doi.org/10.1016/j.ccr.2016.11.002.
[6] W.P. Lustig, S. Mukherjee, N.D. Rudd, A.V. Desai, J. Li, S.K. Ghosh, Chem. Soc. Rev. 46 (2017) 3242–3285, https://doi.org/10.1039/C6CS00930A.
[7] Y. Liu, A.J. Howarth, N.A. Vermeulen, S.-Y. Moon, J.T. Hupp, O.K. Farha, Coord. Chem. Rev. 346 (2017) 101–111, https://doi.org/10.1016/j.ccr.2016.11.008.
[8] P. Falcaro, R. Ricco, A. Yazdi, I. Imaz, S. Furukawa, D. Maspoch, R. Ameloot, J. D. Evans, C.J. Doonan, Coord. Chem. Rev. 307 (2016) 237–254, https://doi.org/10.1016/j.ccr.2015.08.002.
[9] M. Zhang, Z.-Y. Gu, M. Bosch, Z. Perry, H.-C. Zhou, Coord. Chem. Rev. 293–294 (2015) 327–356, https://doi.org/10.1016/j.ccr.2014.05.031.
[10] S.R. Batten, N.R. Champness, X.-M. Chen, J. Garcia-Martinez, S. Kitagawa, L. Öhrström, M. O'Keeffe, M.P. Suh, J. Reedijk, Pure Appl. Chem. 85 (2013) 1715–1724, https://doi.org/10.1351/PAC-REC-12-11-20.
[11] B. Seoane, S. Castellanos, A. Dikhtiarenko, F. Kapteijn, J. Gascon, Coord. Chem. Rev. 307 (2016) 147–187, https://doi.org/10.1016/j.ccr.2015.06.008.
[12] C.R. Murdock, B.C. Hughes, Z. Lu, D.M. Jenkins, Coord. Chem. Rev. 258–259 (2014) 119–136, https://doi.org/10.1016/j.ccr.2013.09.006.
[13] W.-G. Lu, Z.-W. Wei, Z.-Y. Gu, T.-F. Liu, J. Park, J. Park, J. Tian, M.-W. Zhang, Q. Zhang, T. Gentle, M. Bosch, H.-C. Zhou, Chem. Soc. Rev. 43 (2014) 5561–5593, https://doi.org/10.1039/C4CS00003J.
[14] P.C. Lemaire, D.T. Lee, J.J. Zhao, G.N. Parsons, ACS Appl. Mater. Interfaces 9 (2017) 22042–22054, https://doi.org/10.1021/acsami.7b05214.
[15] P.F. Ji, K. Manna, Z. Lin, A. Urban, F.X. Greene, G.X. Lan, W.B. Lin, J. Am. Chem. Soc. 138 (2016) 12234–12242, https://doi.org/10.1021/jacs.6b06759.
[16] S.W. Jaros, M.F.C.G.D. Silva, M. Florek, M.C. Oliveira, P. Smolenski, A.J. L. Pombeiro, A.M. Kirillov, Cryst. Growth Des. 14 (2014) 5408–5417, https://doi.org/10.1021/cg500557r.
[17] P. Manna, S.K. Das, Cryst. Growth Des. 15 (2015) 1407–1421, https://doi.org/10.1021/cg501787m.
[18] L.J. Beeching, C.S. Hawes, D.R. Turnera, S.R. Batten, CrystEngComm 1 (2014) 6459–6468, https://doi.org/10.1039/C4CE00816B.
[19] W. Xu, Z.X. Si, M. Xie, L.X. Zhou, Y.Q. Zheng, Cryst. Growth Des. 17 (2017) 2147–2157, https://doi.org/10.1021/acs.cgd.7b00097.
[20] Y. Kobayashi, K. Honjo, S. Kitagawa, T. Uemura, ACS Appl. Mater. Interfaces 9 (2017) 11373–11379, https://doi.org/10.1021/acsami.6b15936.
[21] R. Ding, C. Huang, J. Lu, J. Wang, C. Song, J. Wu, H. Hou, Y. Fan, Inorg. Chem. 54 (2015) 1405–1413, https://doi.org/10.1021/ic502369y.
[22] M. Garai, K. Maji, V.V. Chernyshev, K. Biradha, Cryst. Growth Des. 16 (2016) 550–554, https://doi.org/10.1021/acs.cgd.5b01624.
[23] J. Wang, C. Bai, H.M. Hua, F. Yuan, G.L. Xue, J. Solid State Chem. 249 (2017) 87–97, https://doi.org/10.1016/j.jssc.2017.02.015.
[24] J.Y. Zhang, J.X. Shi, L.Y. Chen, Q.X. Jia, W. Deng, E.Q. Gao, CrystEngComm 19 (2017) 1738–1750, https://doi.org/10.1039/C7CE00046D.
[25] (a) S. Ghosh, G. Pahari, A. Maiti, S. Dinda, D. Ghoshal, Polyhedron 218 (2022) 115763. doi: 10.1016/j.poly.2022.115763. (b) Z.-X. Xu, M.-F. Shi, Y. Wan, X. Gu, Polyhedron 224 (2022) 116001. doi: 10.1016/j.poly.2022.116001. (c) P.C. Preethi, A. Harisankar, U.S. S. Mol, R. Raghunandan, Polyhedron 223 (2022) 115974. doi: 10.1016/j.poly.2022.115974. (d) G.-L. Wang, Y. Lu, R. Wang, D. Srivastava, A. Kumar, H.-Sakiyama, Mohd. Muddassir, J. Guo, J.-C. Jin, Polyhedron 227 (2022) 116141. doi: 10.1016/j.poly.2022.116141. (e) Y. Zhou, Y.-L. Zhang, Q. Zhang, S.-Y. Yang, X.-Q. Wei, Z. Tian, D. Shao, Polyhedron 225 (2022) 116078. doi: 10.1016/j.poly.2022.116078.
[26] H.I. Hamoud, P. Damacet, D. Fan, N. Assaad, O.I. Lebedev, A. Krystianiak, A. Gouda, O. Heintz, M. Daturi, G. Maurin, M. Hmadeh, M.E. -Roz, J. Am. Chem. Soc. 144 (36) (2022) 16433–16446, https://doi.org/10.1021/jacs.2c04905.
[27] E. Suresh, K. Boopalan, R.V. Jasra, M.M. Bhadbhade, Inorg. Chem. 40 (2001) 4078–4080, https://doi.org/10.1021/ic000434v.
[28] C. Chen, H. Zhu, D. Huang, T. Wen, Q. Liu, D. Liao, J. Cui, Inorg. Chim. Acta 320 (2001) 159–166, https://doi.org/10.1016/S0020-1693(01)00489-3.

[29] S.G. Baca, I.G. Filippova, O.A. Gherco, M. Gdaniec, Y.A. Simonov, N.V. Gerbeleu, P. Franz, R. Basler, S. Decurtins, Inorg. Chim. Acta 357 (2004) 3419–3429, https://doi.org/10.1016/S0020-1693(03)00498-5.
[30] C. Yenikaya, M. Poyraz, M. Sarı, F. Demirci, H. Ilkimen, O. Buyukgungor, Polyhedron 28 (2009) 3526–3532, https://doi.org/10.1016/j.poly.2009.05.079.
[31] M. Odabasoglu, O. Buyukgungor, G. Turgut, A. Karadag, E. Bulak, P. Lonnecke, J. Mol. Struct. 648 (2003) 133–138, https://doi.org/10.1016/S0022-2860(02)00720-2.
[32] R.N. Rao, K. Chanda, Chem. Commun. 58 (2022) 343–382, https://doi.org/10.1039/D1CC04602K.
[33] B. Dojer, P. Andrej, P. Šegedin, Z. Jagličić, Č. Stropnik, M. Kristl, M. Drofenik, Inorg. Chim. Acta 363 (2010) 1343–1347, https://doi.org/10.1016/j.ica.2009.12.052.
[34] L. Li, F. Yuan, Synth. React. Inorg. Met.-Org. Chem. 42 (2012) 205–208, https://doi.org/10.1080/15533174.2011.609518.
[35] S. Nieto, J. Perez, L. Riera, V. Riera, D. Miguel, Chem. Commun. 22 (2009) 3279–3281, https://doi.org/10.1039/B823460D.
[36] N. Kanematsu, M. Ebihara, T. Kawamura, Inorg. Chim. Acta 292 (1999) 244–248, https://doi.org/10.1016/S0020-1693(99)00218-2.
[37] S.M.N. Islam, K.K. Borah, F.E. Öztürkkan, M.A. Raza, A. Frontera, D.M. Gil, J. Mol. Struct. 1268 (2022) 133686–133698, https://doi.org/10.1016/j.molstruc.2022.133686.
[38] (a) S.M.N. Islam, D. Dutta, P. Sharma, A.K. Verma, A. Frontera, M.K. Bhattacharyya, Inorganica Chimica Acta 498 (2019) 119108−119118. doi: 10.1016/j.ica.2019.119108. (b) M.K. Bhattacharyya, D. Dutta, S.M. N. Islama, A. Frontera, P. Sharma, A.K. Verma, A. Das, Inorganica Chimica Acta 501 (2020) 119233−119246. doi: 10.1016/j.ica.2019.119233. (c) S.M.N. Islam, D. Dutta, A.K. Verma, H. Nath, A. Frontera, P. Sharma, M.K. Bhattacharyya, Inorganica Chimica Acta 498 (2019) 119161−119174. doi: 10.1016/j.ica.2019.119161.
[39] Bruker AXS Inc., Madison, Wisconsin, USA, 2007.
[40] Bruker AXS Inc., Programme Name (s), Madison, Wisconsin, USA. 2001.
[41] G.M. Sheldrick, Acta Crystallogr. A 64 (2008) 112–122.
[42] L.J. Farrugia, J. Appl. Crystallogr 32 (1999) 837–838.
[43] K. Brandenburg, Diamond: Visual Crystal Structure Information System (Version 3.1f), Crystal Impact GbR, Bonn, 2008.
[44] D. Tatlidil, M.A. Raza, N. Dege, A.A. Agar, U. Farwa, S.U. Rehman, ACS Omega 7 (2022) 10568–10579, https://doi.org/10.1021/acsomega.2c00102.
[45] M.A. Raza, K. Fatima, J. Phys. Org. Chem. 33 (10) (2020) e4076, https://doi.org/10.1002/poc.4076.
[46] M. Danish, A. Bibi, K. Gilani, M.A. Raza, M. Ashfaq, M.N. Arshad, A.M. Asiri, K. Ayub, J. Mol. Struct. 1175 (2019) 379–388, https://doi.org/10.1016/j.molstruc.2018.07.116.
[47] A. Daina, O. Michielin, V. Zoete, SwissADME: a free web tool to evaluate pharmacokinetics, drug-likeness and medicinal chemistry friendliness of small molecules, Sci. Rep. 7 (2017) 42717, https://doi.org/10.1038/srep42717.
[48] P. Banerjee, A.O. Eckert, A.K. Schrey, R. Preissner, ProTox-II: a web server for the prediction of toxicity of chemicals, Nucl. AcidsRes. 46 (2018) W257–W263, https://doi.org/10.1093/nar/gky318.
[49] D. Mannar, J.W. Saville, X. Zhu, S.S. Srivastava, A.M. Berezuk, K.S. Tuttle, A. C. Marquez, I. Sekirov, S. Subramaniam, Science 375 (2022) 760–764, https://doi.org/10.1126/science.abn7760.
[50] Z. Jin, X. Du, Y. Xu, Y. Deng, M. Liu, Y. Zhao, B. Zhang, X. Li, L. Zhang, C. Peng, Y. Duan, J. Yu, L. Wang, K. Yang, F. Liu, R. Jiang, X. Yang, T. You, X. Liu, X. Yang, F. Bai, H. Liu, X. Liu, L.W. Guddat, W. Xu, G. Xiao, C. Qin, Z. Shi, H. Jiang, Z. Rao, H. Yang, Nature 582 (2020) 289–293, https://doi.org/10.1038/s41586-020-2223-y.
[51] W. Yin, C. Mao, X. Luan, D.-.-D. Shen, Q. Shen, H. Su, X. Wang, F. Zhou, W. Zhao, M. Gao, S. Chang, Y.C. Xie, G. Tian, H.W. Jiang, S.C. Tao, J. Shen, Y. Jiang, H. Jiang, Y. Xu, S. Zhang, Y. Zhang, H.E. Xu, Science 368 (2020) 1499–1504, https://doi.org/10.1126/science.abc1560.
[52] Y. Kim, J. Wower, N. Maltseva, C. Chang, R. Jedrzejczak, M. Wilamowski, S. Kang, V. Nicolaescu, G. Randall, K. Michalska, A. Joachimiak, Commun. Biol. 4 (2021) 1–11, https://doi.org/10.1038/s42003-021-01735-9.
[53] M. Rosas-Lemus, G. Minasov, L. Shuvalova, N.L. Inniss, O. Kiryukhina, J. Brunzelle, K.J.F. Satchell, Sci. Signal. 13 (2020) eabe1202, https://doi.org/10.1126/scisignal.abe1202.
[54] B.J. Fraser, S. Beldar, A. Seitova, A. Hutchinson, D. Mannar, Y. Li, D. Kwon, R. Tan, R.P. Wilson, K. Leopold, S. Subramaniam, L. Halabelian, C.H. Arrowsmith, François Bénard, Nat. Chem. Biol. 18 (2022) 963–971, https://doi.org/10.1038/s41589-022-01059-7.
[55] O. Trott, A.J. Olson, J. Comput. Chem. (2009) 455–461, https://doi.org/10.1002/jcc.21334.
[56] BIOVIA, DassaultSystèmes, BIOVA Discovery Studio Visualizer 2021, v21.1.0.20298, San Diego: DassaultSystèmes, 2021.
[57] (a) L.J. Bellamy, The Infrared Spectra of Complex Molecules, 2, second ed., Chapman & Hall, London/New York, 1980;
(b) K. Nakamoto, Infrared and Raman Spectra of Inorganic and Coordination Compounds, fifth ed., John Wiley & Sons, New York, 1997.
[58] (a) B. Ay, E. Yildiz, I. Kani, J. Solid State Chem. 233 (2016) 44–51. doi: 10.1016/j.jssc.2015.09.036. (b) L. Yang, L. Liu, L. Wu, H. Zhang, S. Song, Dyes Pigments 105 (2014) 180–191. doi: 10.1016/j.dyepig.2014.01.032.
[59] (a) C. Yenikaya, M. Poyraz, M. Sarı, F. Demirci, H. Ilkimen, O. Buyukgungor, Polyhedron 28 (2009) 3526–3532. doi: 10.1016/j.poly.2009.05.079. (b) F. Erdemir, D.B. Celepci, A. Aktaş, Y. Gök, R. Kaya, P. Taslimi, Y. Demir, I. Gulçin, Bioorg. Chem. 91 (2019) 103134–103154. doi: 10.1016/j.bioorg. 2019.103134.
[60] L. Yang, D.R. Powell, R.P. Houser, Dalton Trans. 955 (2007) 955–964, https://doi.org/10.1039/B617136B.
[61] (a) L. Mei, T.H. Ming, L.Q. Rong, S. Jie, Y.S. Zhong, L.X. Liang, J. Chem. Sci. 121 (2009) 435–440. (b) D. Sun, Z-H. Yan, V.A. Blatov, L. Wang, D-F. Sun, Cryst. Growth Des. 13 (2013) 1277−1289. doi: 10.1021/cg3017358.
[62] N. Dege, M.A. Raza, O.E. Doğan, T. Ağar, M.W. Mumtaz, J. Iran. Chem. Soc. 18 (2021) 2345–2368, https://doi.org/10.1007/s13738-021-02194-z.
[63] M.A. Raza, D. Necmi, O.E. DOĞAN, A. Tuğgan, S.H. Sumrra, J. Mol. Struct. 1226 (2021), 129330, https://doi.org/10.1016/j.molstruc.2020.129330.
[64] M. Ashfaq, G. Bogdanov, A. Ali, M.N. Tahir, S. Abdullah, J. Mol. Struct. 1235 (2021) 130215–130221, https://doi.org/10.1016/j.molstruc.2021.130215.
[65] P.K. Devi, K. Venkatachalam, M. Poonkothai, J. Mol. Struct. 1119 (2016) 462–471, https://doi.org/10.1016/j.molstruc.2016.05.001.
[66] P. Politzer, J.S. Murray, Theor. Chimi. Acta 108 (2002) 134–142, https://doi.org/10.1007/s00214-002-0363-9.
[67] C.A. Lipinski, F. Lombardo, B.W. Dominy, P.J. Feeney, Adv. DrugDeliv. Rev. 23 (1997) 3–25, https://doi.org/10.1016/S0169-409X(96)00423-1.
[68] J. Haribabu, N. Balakrishnan, S. Swaminathan, J. Peter, D. Gayathri, C. Echeverria, N. Bhuvanesh, R. Karvembu, Inorg. Chem. Commun. 134 (2021) 109029–109039, https://doi.org/10.1016/j.inoche.2021.109029.
[69] T.W. Murinzi, E. Hosten, G.M. Watkins, Polyhedron 137 (2017) 188–196, https://doi.org/10.1016/j.poly.2017.08.030.